

Line identification of extreme ultraviolet spectra from aluminum ions in EAST Tokamak plasmas

Fengling Zhang^{1,2}, Darío Mitnik^{*3,1}, Ling Zhang^{†1}, Wenming Zhang^{1,2}, Yunxin Cheng¹, Ailan Hu¹, Xiaobin Ding⁴, Shigeru Morita⁵, Zhengwei Li^{1,6}, Zhen Zhou^{1,2}, Yiming Cao^{1,6}, Jiuyang Ma^{1,2}, Zhehao Xu^{1,6}, Lang Xu^{1,2}, Chenxi Zhou², and Yinxian Jie¹

¹ Institute of Plasma Physics, Hefei Institutes of Physical Science, Chinese Academy of Sciences, Hefei 230031, China

² University of Science and Technology of China, Hefei 230026, China

³ Instituto de Astronomía y Física del Espacio (CONICET-Universidad de Buenos Aires), Buenos Aires 1428, Argentina

⁴ Key Laboratory of Atomic and Molecular Physics and Functional Materials of Gansu Province, College of Physics and Electronic Engineering, Northwest Normal University, Lanzhou 730070, China

⁵ National Institute for Fusion Science, Toki 509-5292, Gifu, Japan

⁶ Anhui University, Hefei 230601, China

E-mail: *dmitnik@df.uba.ar, †zhangling@ipp.ac.cn

August 2023

Abstract.

Extreme ultraviolet (EUV) spectra emitted from aluminum in the 5–340 Å wavelength range were observed in Experimental Advanced Superconducting Tokamak (EAST) discharges. Several spectral lines from aluminum ions with different degrees of ionization were successfully observed with sufficient spectral intensities and resolutions using three fast-time-response EUV spectrometers. The line identification uses three independent state-of-art computational codes for the atomic structure calculations, which provide the wavelengths and radiative transition probabilities rate coefficients. These programs are HULLAC (Hebrew University - Lawrence Livermore Atomic Code), AUTOSTRUCTURE, and FAC (Flexible Atomic Code). Using three different codes allows us to resolve some ambiguities in identifying certain spectral lines and assess the validity of the theoretical predictions.

Keywords: plasma spectroscopy, Tokamak spectra, relativistic atomic structure
Submitted to: *Phys. Scr.*

1. INTRODUCTION

In magnetic confinement fusion Tokamak devices, there are usually various impurities in addition to the working particles. The primary sources of them are due to the interaction between the edge plasma and plasma-facing components (PFCs), like sputtering [1, 2] and desorption [3] processes. Impurities can penetrate the central plasma causing significant power losses, diluting the fuel ions, and disrupting the steady-state operation of the plasma. Therefore, spectroscopic measurements of line emissions from impurity ions are crucial to monitor their behavior and minimize their effects on plasma performance.

The Experimental Advanced Superconducting Tokamak (EAST) is an advanced steady-state plasma device described in several reports (see, for example, [4, 5, 6, 7]). Various PFCs are located in different regions of EAST, protecting the vacuum vessel, the heating systems, and the diagnostic components from the plasma particles and heat loads [8]. Examples of PFC are the tungsten divertors [8, 7], the first wall made of molybdenum bricks [8], the tungsten blocks assembly with CuCrZr employed in the guard limiter for the lower hybrid waveguide antennas [9, 10], the carbon bricks where the neutral beam injection (NBI) is deposited [11], and other physical diagnostic systems installed on the vacuum chamber wall. In addition, high-temperature resistant alumina ceramic Al_2O_3 blocks are found in the magnetic probes [12, 13, 14].

In our previous works, we have observed and identified the EUV spectra of low-Z impurities [15] such as helium, lithium, boron, carbon, oxygen, neon, silicon, argon, and high-Z impurities [16, 17] such as iron, copper, molybdenum, and tungsten. We used two sets of fast-time-response EUV spectrometers [18, 19] called ‘EUV_Short’ and ‘EUV_Long’ working at 8-130 Å and 20-500 Å. In that way, we have established a primary database of impurity EUV spectra in EAST plasma. However, in these spectra, we still found some unrecognized lines that did not come from the impurity elements which have been identified. Using several high-intensity spectral lines of intrinsic low-Z impurities for calibration, through careful comparison and analysis with relevant literature, it was found that the unrecognized spectral lines are consistent with the spectrum of aluminum ions.

Valero and Goorvitch reported spectral lines of Al VI to Al X ions in the range of 48 to 335 Å in laser-produced plasma experiments [20]. Other laser-produced plasma experiments have also observed resonant transition lines of aluminum hydrogen-like [21, 22] and helium-like [23, 24, 25] aluminum ions. Gu et al. [26] observed aluminum ions’s L-shell emission spectra in the 40-170 Å range in the Livermore electron beam ion trap (EBIT) device. They identified the lines by using a detailed collisional-radiative (CR) model. In addition, the EUV spectra of highly ionized aluminum ions have been observed during a laser blow-off experiment using an aluminum target for an NBI-heated plasma created in the TJ-II stellarator [27]. However, they only observed lines with wavelengths higher than 175 Å.

From the theoretical point of view, aluminum is an interesting case. On the one

hand, the structure of its ions requires the inclusion of coupling between the different degrees of ionization (therefore, the calculation of complex processes such as dielectronic recombination or excitation-autoionization). Many ion stages and many levels for each one of these ions must be included for any individual ion calculation. The matrices involved are so large that it is generally necessary to develop approximation methods in which some excited states can be grouped in bundled configurations, reproducing thus the same effects as in the explicit level-by-level calculation. If insufficient to allow the computations, each ion stage should be considered separately or connected only with a few neighboring ions. On the other hand, the aluminum ions system is not prohibitively complex, so we are facing the task of performing an explicit and detailed collisional-radiative model (CRM) calculation allowing us to assess the different approximation methods. That will be described in a forthcoming article. In the present work, the first required step of identification of the lines, based on a simple and preliminary collisional radiative model, is performed. To that end, we employed three different atomic structure computational codes described briefly in Section 3. That allows us to identify with certainty the aluminum spectral lines, as detailed in Section 4.

2. Experimental setup

During the EAST upgrade in 2021 [28], two new fast EUV spectrometers were supplemented the previous set, making up a total of four fast EUV spectrometers, namely EUV_Short, EUV_Long_a, EUV_Long_b, and EUV_Long_c. All the spectrometers are equipped with a laminar-type varied-line-spacing concave holographic grating (1200 and 2400 grooves/mm for long and short, respectively). They are fixed at grazing incidence (angle of incidence about 87.0°) with a narrow entrance slit width of $30\ \mu\text{m}$ to increase the spectral resolution. A back-illuminated charge-coupled detector (CCD) with a sensitive area of $26.6 \times 6.6\ \text{mm}^2$ (1024×255 pixels, $26 \times 26\ \mu\text{m}^2/\text{pixel}$) is used for recording the spectral image. For the standard definition of resolution, full width at half maximum (FWHM), the spectral resolution is 0.1 at $20\ \text{\AA}$ [19], $0.22\ \text{\AA}$ at $100\ \text{\AA}$, and $0.30\ \text{\AA}$ at $200\ \text{\AA}$ [18]. The spectra are recorded every $5\ \text{ms}$ when the CCD is operated with full vertical binning mode. Previously, the two spectrometers needed to adjust the stepper motor to control the CCD's position and change the wavelength's observation range. Now, the four spectrometers have achieved full coverage in the $5\text{-}500\ \text{\AA}$ band without changing the CCD position. In the present experiment, the EUV_Long_c spectrometer was not operating; therefore, we analyzed only the $5\text{-}380\ \text{\AA}$ band. The wavelength calibration is performed by cubic polynomial fitting with many well-known spectral lines covering the observable range [15]. The line of sight (LOS) for the other three spectrometers is indicated with the EAST plasma cross-section in Fig. 1.

Once we establish that unknown spectral lines can come from the Al presence, the next step is to look at the temporal behavior of some dominant lines of their different ions. An illustrative example is in Fig. 2, where the Al lines arise in a spontaneous

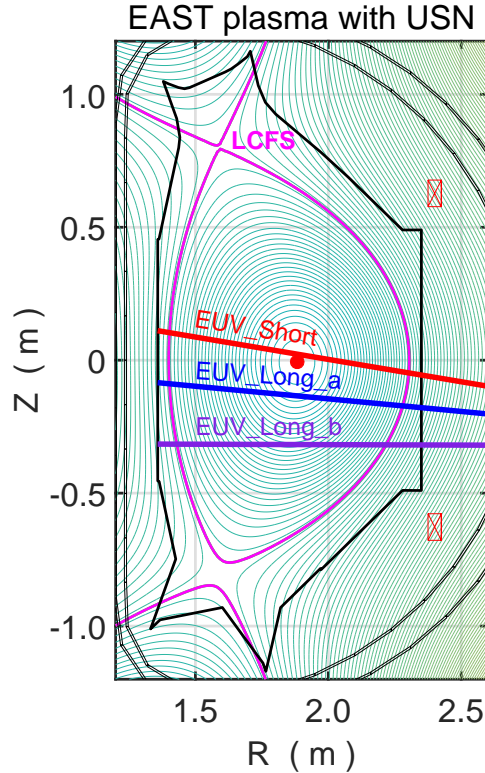


Figure 1. LOS of the two fast-time-response EUV spectrometers. Red line: EUV_Short. Blue line: EUV_Long_a. Purple line: EUV_Long_b.

sputtering event during the EAST 108709 discharge. A sudden increase in the intensities of the Al spectral lines occurred at 6.885 seconds, reached a maximum, and then returned to the average value after 15 ms. The precise time of the maximum intensities depends on the ionization degree, being $t = 6.890$ s for the lower charges (Al^{3+} to Al^{5+}) and $t = 6.895$ for the other ions, except Al^{12+} , in which the maximum intensity arises at $t = 6.900$ s.

The emission lines corresponding to the Al ions can be easily found by the comparison of the spectra obtained before ($t < 6.890$ s) and during ($t = 6.895$ s) the Al burst, as is shown in Figure 3. In this particular discharge, the electron temperature of the plasma core was $T_e(0) = 2.5$ keV, and the chord-average electron density $n_e = 2.6 \times 10^{19} \text{ m}^{-3}$. Both parameters have been provided by a Thomson scattering system [29] and reflectometer measurements [30].

Figure 4 shows the aluminum spectra observed in the 5-340 Å band. In this, we identify many lines belonging to Li, C, and especially O ions. These strong lines were used in the calibration method. As is shown in the Figure, the highly ionized Al (H- and He-like) only contribute to the spectra at short wavelengths, and most of the Al lines appear between 50 Å and 135 Å. The dominant lines around 160 Å belong to Al^{3+} . We are not plotting the spectra beyond 340 Å since the intensities are very small. In Section 4, we will provide a detailed analysis of all the lines that we have been able to identify with certainty.

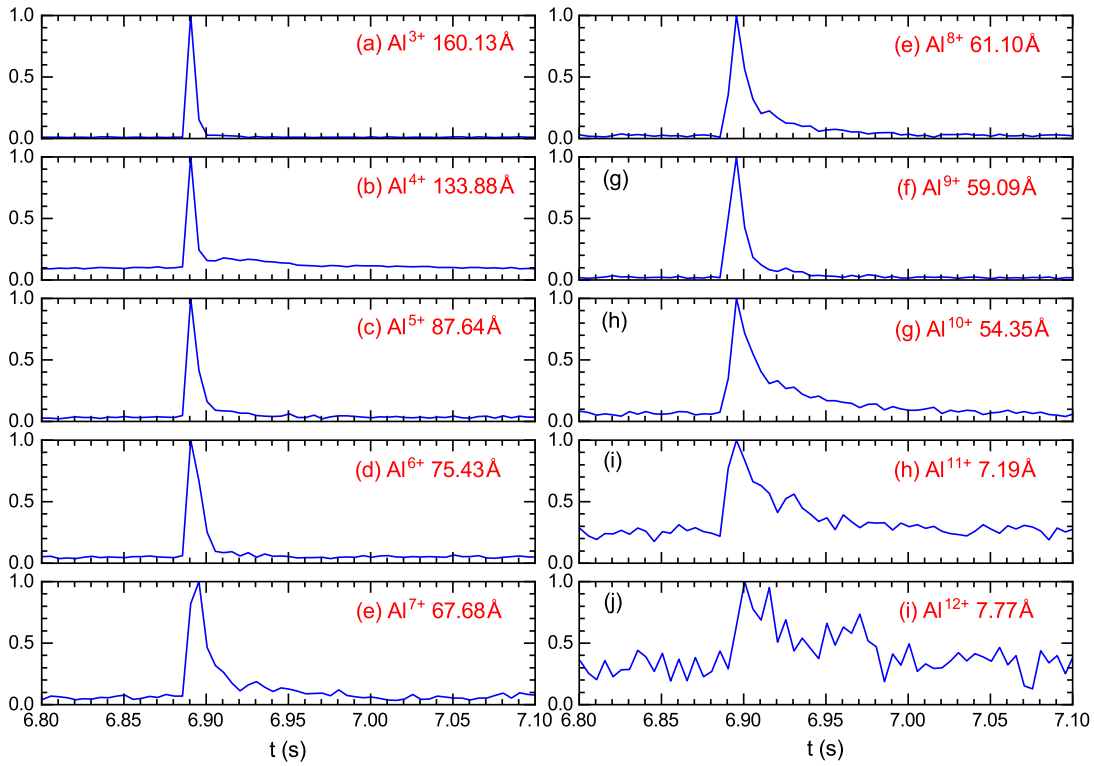


Figure 2. Time evolution of the Al³⁺ to Al¹²⁺ dominant lines emission during the EAST 108709 discharge.

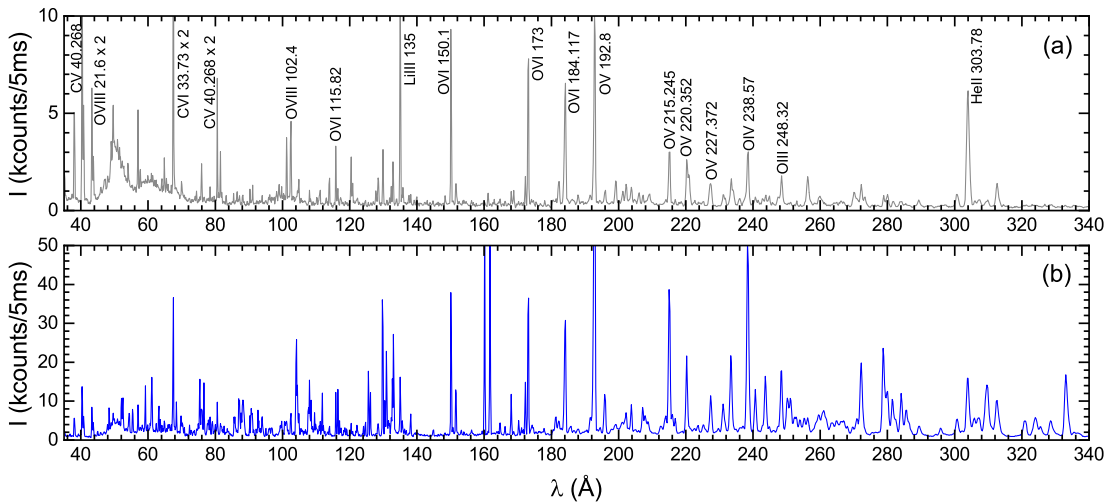


Figure 3. Full spectra of the EAST 108709 discharge taken (a) at time $t < 6.890$ s, before the Al burst, and (b) at $t = 6.895$ s, when the Al intensity reaches the maximum value.

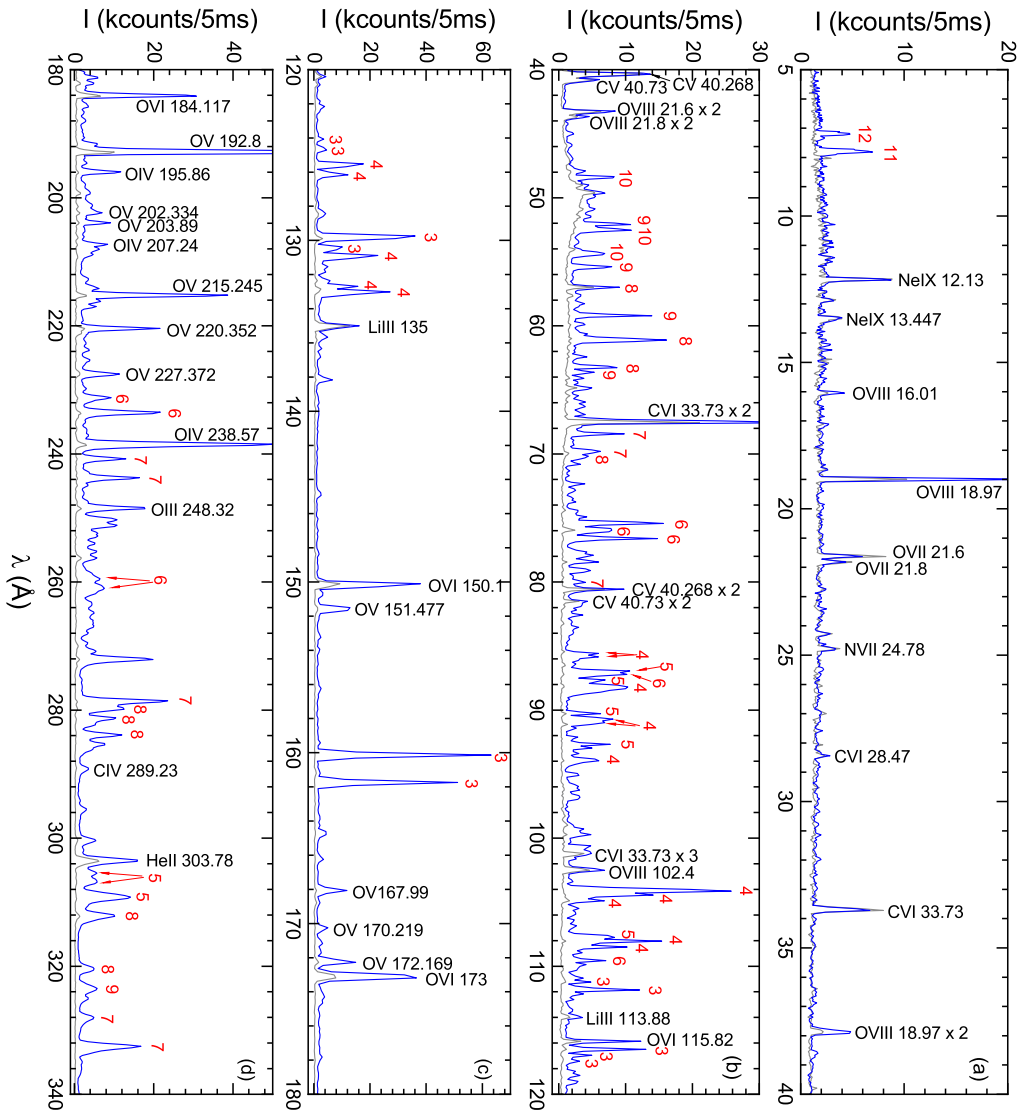


Figure 4. EUV spectra observed in the EAST experiment and lines identified as belonging to aluminum ions (red labels). The numbers n means that the corresponding ion is Al^{n+} . gray curve: spectrum before the Al burst. Blue curve: spectra at maximum Al emission.

3. Theoretical methods

The spectral lines have been identified with three separate independent calculations. We used the atomic structure computational codes HULLAC (Hebrew University - Lawrence Livermore Atomic Code) [31, 32, 31], the AS (AutoStructure) code [33, 34, 35], and the FAC (Flexible Atomic Code) [36].

Since the three codes are very well-known in astrophysics and fusion communities, we only briefly summarize their main features. HULLAC is a fully relativistic atomic structure package of codes that provides the transition energies and the corresponding rate coefficients, among other quantities. The code implements the relativistic parameter potential method to solve the Dirac Hamiltonian. Full multiconfiguration wavefunctions are used to compute the radiative transition rates; thus, configuration mixing, and therefore, correlation effects, are included in the calculations. The Breit interaction and quantum electrodynamic (vacuum polarization and the self-energy) corrections are treated as second-order perturbations. The AutoStructure code allows calculating energy levels, oscillator strengths, excitation, photoionization cross sections, and autoionization rates, among other quantities. These can be calculated with configuration resolution (configuration average CA), term resolution (LS coupling), or level resolution (intermediate coupling IC) using semi-relativistic kappa-averaged wavefunctions. It also allows the inclusion of mixing configurations. FAC employs a fully relativistic approach, solving the Dirac equation. Quantum-electrodynamic effects, mainly arising from Breit interaction, vacuum polarization, and electron self-energy are all included with standard procedures in the code. Like the other programs mentioned, FAC has been widely employed to interpret laboratory and astrophysical spectroscopic data.

The present work allows us to compare the results obtained with these three codes and evaluate their accuracy. The general agreement between them is very good; roughly, the wavelengths differ by a factor close to 2 Å. Although the codes allow us to adjust the energies with experimental values, we prefer to show the comparisons in an unrefined form, to get a glimpse of the reliability of the basic calculations. As an example, we show, in Fig. 5, more than 16000 transition lines corresponding to the Al³⁺ ion. The Figure shows only the radiative transition rate coefficients. A further detailed CR model is needed to compare with the experimental spectra. This task will be addressed in a forthcoming work.

4. Spectra of Aluminum ions

4.1. Al³⁺

The Al³⁺ ion is isoelectronic to the Ne; its ground configuration is 1s²2s²2p⁶. Since it is a closed-shell ion, its ionization energy is relatively high (119.99 eV) compared to the neighboring ion stages. Therefore, it is supposed to have a large and broad predominance in the fractional abundances distribution (in this case, around 10 eV)

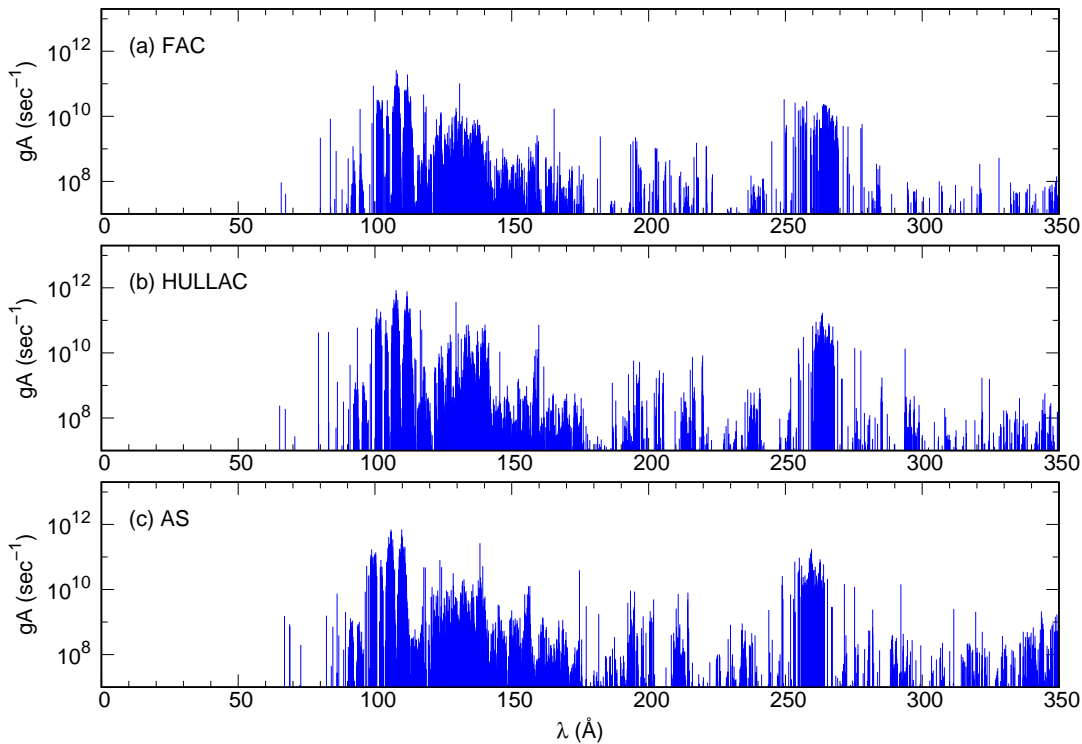


Figure 5. Comparisons of radiative transition rate coefficients for Al^{3+} calculated by (a) FAC, (b) HULLAC, and (c) AS.

over a wide range of temperatures. Based on the spectral characteristics of Al^{3+} ion described in the EBIT experiment [26] as well as the wavelength values reported in the NIST database, we have managed to identify 12 spectral lines in the tokamak spectra, which we show in Fig. 6.

For the theoretical calculations, we include in our model, besides the ground configuration $2s^22p^6$, the $2s^22p^5nl$ ($n = 3, 4, 5$), $2s^22p^43l^2$, and the $2s2p^6nl$ ($n = 3, 4, 5$) configurations, including all the mixing between these configurations. The resultant structure has 366 levels. Due to both the existence of strong transitions and the low charge of the ion, only electron dipole-allowed transitions have been considered, resulting in more than 16000 radiative rates. In this system, the transitions with the largest radiative rate coefficients are the $2s^22p^43d^2 \rightarrow 2s^22p^53d$, with wavelengths close to 110 Å and Einstein coefficient values of about 10^{11} s^{-1} . However, a preliminary collisional radiative model shows that the upper levels of these transitions are insufficiently populated to produce a significant contribution to the spectra. The transitions $2s2p^6nl \rightarrow 2s^22p^6$, with wavelengths shorter than 100 Å and high radiative rate coefficients, do not appear in the tokamak spectra. This is probably because these levels are above the ionization limit, allowing autoionization channels that effectively quench the radiative path. All these speculations must be validated with a detailed and complete collisional-radiative model, which exceeds the objectives of this work, and which we will present in a forthcoming publication. The next important transitions

are from the odd configurations having a hole in the $2p$ shell to the ground state, i.e., $(2p^5nl)_{J=1} \rightarrow 2p^6$. These transitions produce the prominent lines observed in the spectra, marked in Figure 6 and described in Table 1. Some are blended with other ion's lines and cannot be identified with certainty. These are labeled with an asterisk, for example, line 9*, which appears at the same wavelength as a $2p^63s \rightarrow 2p^5$ transition from Al^{4+} (line 14* in Table 2). The wrap-up of our observations and preparatory calculations shows that the Al^{3+} spectra can be characterized by three strong transitions, the $3d \rightarrow 2p$ labeled as 8 in the Table, and the last two $3s \rightarrow 2p$ labeled as 10 and 11. As is shown in the Table, both FAC and AS calculations are in very good agreement with the experimental results, between a 2 \AA error range. For some reason, FAC generally predicts wavelengths higher than the experimental values, whereas AS results are below the measurements. The results obtained with HULLAC are in remarkable agreement with the experimental values, with less than a 0.3% discrepancy between them in most cases.

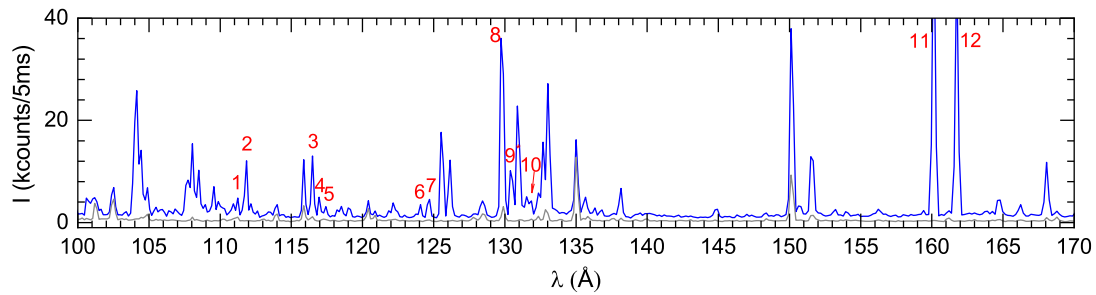


Figure 6. EAST spectrum and the lines identified as belonging to Al^{3+} . The numbers indicate the lines (Key) described in Table 1.

Table 1. EAST experimental (Exp.) and theoretical lines (FAC, HULLAC, and AUTOSTRUCTURE), for Al^{3+} . The values from other experiments and the values quoted in NIST are also displayed. The column ‘Key’ indicates the transitions labeled in Fig. 6. The symbol * means that the line is blended with another ion’s line, as explained in the text. We use the usual relativistic nomenclature $j_{\pm} \equiv l \pm \frac{1}{2}$. The last subscript means the total J quantum number of the level.

Key	Exp.	FAC	HULLAC	AS	Previous Exp.	NIST	Lower	Upper
1	111.24	112.49	111.36	109.74	111.301 ^a	111.196	$2p^6$	$(2p^1_2 2p^4_1 5d_-)_1$
2	111.85	112.90	111.77	110.22	111.711 ^a	111.781	$2p^6$	$(2p^2_2 2p^3_1 5d_+)_1$
3	116.49	117.76	116.56	114.80	116.546 ^a	116.464	$2p^6$	$(2p^1_2 2p^4_1 4d_-)_1$
4	116.96	118.29	117.08	115.42	117.070 ^a	116.921	$2p^6$	$(2p^2_2 2p^3_1 4d_+)_1$
5	117.42	118.76	117.55	115.95		117.377	$2p^6$	$(2p^2_2 2p^3_1 4d_-)_1$
6	124.07	125.49	124.18	122.39	124.097 ^a	124.030	$2p^6$	$(2p^1_2 2p^4_1 4s)_1$
7	124.71	126.02	124.70	122.98	124.619 ^a	124.550	$2p^6$	$(2p^2_2 2p^3_1 4s)_1$
8	129.73	130.95	129.57	127.46	129.793 ^a	129.730	$2p^6$	$(2p^1_2 2p^4_1 3d_-)_1$
9*	130.39	131.89	130.40	128.47	130.473 ^a	130.39	$2p^6$	$(2p^2_2 2p^3_1 3d_+)_1$
10	131.86	133.30	131.72	129.91		131.647	$2p^6$	$(2p^2_2 2p^3_1 3d_-)_1$
11	160.13	162.44	159.79	158.84	160.089 ^a	160.074	$2p^6$	$(2p^1_2 2p^4_1 3s)_1$
12	161.74	164.61	161.64	160.70	161.712 ^a	161.688	$2p^6$	$(2p^2_2 2p^3_1 3s)_1$

^a Livermore EBIT experimental results [26].

4.2. Al^{4+}

The Al^{4+} ion is isoelectronic to the F, having a ground configuration $1s^2 2s^2 2p^5$. The ionization energy is about 152 eV; however, its maximum abundance is roughly predicted to be around 20 eV. As in the previous case, the transitions with the highest radiative rate coefficients do not necessarily dominate the spectrum. Here, the transitions $2s^2 2p^3 3d^2$ to $2s^2 2p^4 3d$ (i.e., $3d \rightarrow 2p$) and $2s 2p^5 4d$ to $2s 2p^6$ ($4d \rightarrow 2p$) have the largest Einstein coefficients, of the order of 10^{11} s^{-1} . Lines belonging to the first group should appear at 90.1 Å and 94.2 Å, and to the second, around 96.8 Å. However, our collisional-radiative model shows that the upper levels of these transitions are not populated. Indeed, as is shown in Fig. 7, these lines are hardly seen in the spectrum. This Figure shows the region of the EAST spectra in which it is possible to identify 18 lines corresponding to Al^{4+} ion transitions. These lines are described in Table 2, and again, the experimental results are compared with EBIT results, NIST tabulated data, and our theoretical calculation results given by FAC, HULLAC, and AS. For the identification, we included in our theoretical model the ground $1s^2 2s^2 2p^5$ configuration, and $1s^2 2s^2 2p^4 nl$ ($n = 3, 4, 5$), $1s^2 2s 2p^5 nl$ ($n = 3, 4, 5$), $1s^2 2s^2 2p^3 3l^2$, $1s^2 2s^2 2p^3 3s 3p$, and $1s^2 2s 2p^6$ configurations, amounting to 740 levels, and about 75000 dipole-allowed radiative transitions. Line identification is more difficult than other cases, because different transitions overlap in the same region. The Table shows that most of the prominent lines correspond to decay to the ground configuration. The Al^{4+} spectrum consists of four easily identifiable regions. The first one (between 85 and 95 Å) contains the $nd \rightarrow 2p$ transitions listed in the Table as 1-6 lines. These lines are blended with a similar group of lines belonging to the Al^{5+} ion. A noticeable structure of three pronounced peaks between 104 and 105 Å corresponds to the $4d \rightarrow 2p$ transitions (lines 7*, 8*, and 9 in the Table). Although our calculations allow line identification, we obtained the same features for the Al^{5+} ion, overlapping at the same place (lines 5* and 6* in Table 3). The third group of lines has the $3d \rightarrow 2p$ transitions (10-11), which are strong but not very well isolated. The last group of Al^{4+} lines covers the region 125-133 Å and is formed by $3s \rightarrow 2p$ lines (lines 12 to 18). These are striking and identifiable lines. As in the previous case, we found good agreement between the theoretical predictions and the experimental results. Again, FAC wavelengths are slightly higher than the experimental values, whereas AS results are below the measurements. Also, the HULLAC results are in excellent agreement with the experimental values, about in the 0.5% range of discrepancy.

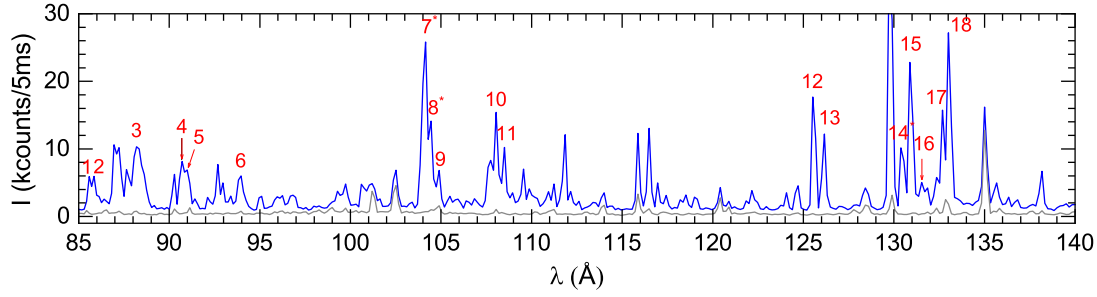


Figure 7. EAST spectrum and the lines identified as belonging to Al^{4+} . The numbers indicate the lines (Key) described in Table 2.

Table 2. EAST experimental and theoretical lines (FAC, HULLAC, and AUTOSTRUCTURE), for Al^{4+} . The values from other experiments and the values quoted in NIST are also displayed. The column ‘Key’ indicates the transitions labeled in Fig. 7. The symbol * means that the line is blended with another ion’s line, as explained in the text. We use the usual relativistic nomenclature $j_{\pm} \equiv l \pm \frac{1}{2}$.

Key	Exp.	FAC	HULLAC	AS	Previous Exp.	NIST	Lower	Upper
1	85.58	86.28	85.59	85.30	85.817 ^a	85.804	$2p_{+}^{5}$	$(2p_{-}2p_{+}^{3}5d_{-})_{3/2}$
2	85.85	86.50	85.84	85.39		85.922	$2p_{-}^{5}$	$(2p_{-}2p_{+}^{3}5d_{+})_{3/2}$
3	88.20	89.27	88.67	87.46	88.480 ^a	88.539	$2p_{-}^{5}$	$(2p_{+}^{4}5d_{-})_{3/2}$
4	90.71	91.34	90.58	90.22	90.889 ^a	90.701	$2p_{+}^{5}$	$(2p_{-}2p_{+}^{3}4d_{-})_{5/2}$
5	90.99	91.42	90.85	90.47		90.982	$2p_{+}^{5}$	$(2p_{-}2p_{+}^{3}4d_{+})_{3/2}$
6	93.96	94.41	93.75	94.59	94.024 ^a	93.755	$2p_{+}^{5}$	$(2p_{-}2p_{+}^{3}4d_{-})_{5/2}$
7*	104.15	104.84	104.01	103.27	104.196 ^a	104.072	$2p_{-}^{5}$	$(2p_{-}2p_{+}^{3}3d_{+})_{1/2}$
8*	104.45	105.13	104.10	103.57		104.362	$2p_{-}^{5}$	$(2p_{-}2p_{+}^{3}3d_{-})_{1/2}$
9	104.89	105.13	104.12	103.86		104.362	$2p_{-}^{5}$	$(2p_{-}2p_{+}^{3}3d_{+})_{3/2}$
10	108.05	109.14	108.17	108.18	108.072 ^a	108.005	$2p_{+}^{5}$	$(2p_{-}2p_{+}^{3}3d_{+})_{5/2}$
11	108.50	109.15	108.91	108.39	108.587 ^a	108.462	$2p_{-}^{5}$	$(2p_{-}^{2}2p_{+}^{3}3d_{-})_{3/2}$
12	125.52	126.80	125.14	126.65	125.598 ^a	125.529	$2p_{+}^{5}$	$(2p_{-}2p_{+}^{3}3s)_{5/2}$
13	126.16	127.33	125.65	127.10	126.140 ^a 126.05 ^b	126.068	$2p_{-}^{5}$	$(2p_{-}2p_{+}^{3}3s)_{3/2}$
14*	130.39	131.33			130.475 ^a	130.390	$2p_{+}^{5}$	$(2p_{-}^{2}2p_{+}^{3}3s)_{3/2}$
15	130.88	131.79	130.75	129.14	130.944 ^a 130.848 ^b	131.002	$2p_{+}^{5}$	$(2p_{-}2p_{+}^{3}3s)_{1/2}$
16	131.53	131.92	131.17	129.52	131.532 ^a	131.438	$2p_{-}^{5}$	$(2p_{-}^{2}2p_{+}^{3}3s)_{3/2}$
17	132.68	132.38	132.74	130.15	132.964 ^a	132.626	$2p_{+}^{5}$	$(2p_{-}2p_{+}^{3}3s)_{3/2}$
18	133.01	134.24	133.09	130.56		133.233	$2p_{+}^{5}$	$(2p_{+}^{4}3s)_{1/2}$

^a Livermore EBIT experimental results [26].

^b Laser-produced plasma experimental results [20].

4.3. Al^{5+}

The Al^{5+} ion is isoelectronic to O; its ground configuration is $1s^2 2s^2 2p^4$. The first ionization limit is 188.8 eV, and the maximum fractional abundance of this ion is around 30 eV. For the theoretical calculations, we include in our model the $2s^2 2p^3 nl$ ($n = 3, 4, 5$), $2s^2 2p^2 3l^2$, $2s^2 2p^2 3s 3p$, $2s 2p^5$ and the $2s 2p^4 nl$ ($n = 3, 4, 5$) configurations, taking into account all the mixing between these configurations. The resultant structure has 1088 levels. Only the electron-dipole allowed ones have been considered from a total of 6×10^5 transitions, resulting in more than 150000 radiative rate coefficients. In this system, the transitions with the highest radiative rate coefficients are the $2s^2 2p^2 3d^2 \rightarrow 2s^2 2p^3 3d$, with wavelengths close to the 75-78.5 Å, and Einstein coefficient values of about $5 \times 10^{11} \text{ s}^{-1}$. However, the lines appearing in that region of the experimental spectra belong to the Al^{6+} ion. The EAST spectrum is shown in Fig. 8, and the experimental and theoretical results for 12 lines of this ion are shown in Table 3. The spectrum of Al^{5+} ion consists of a first group of lines located between 87 Å and 93 Å. Many of these lines belong to the $2s^2 2p^3 3d \rightarrow 2s^2 2p^4$ transitions, but only some of them can be identified with certainty (lines 1 to 4 in the Table). The next group of lines, between 102 Å and 110 Å, corresponds to the $2s^2 2p^3 3s \rightarrow 2s^2 2p^4$ transitions. As pointed out above, the Al^{4+} and Al^{5+} lines coexist at this region, and the calculations of both ions reproduced the same features. Next, we found theoretically a huge line at 236 Å, corresponding to the transition from the $2s^2 p^4$ to the fourth level of the ground configuration ($2p \rightarrow 2s$ transition), which is missing in the experimental spectrum. We included more configuration interactions in the calculations, adding $2s^2 2p^3 nl$ and $2s 2p^4 nl$ ($n = 6, 7$) to investigate the possibility of shifting the position of the lines towards one of the closest experimental peaks. However, the changes are not relevant for this line identification. We do not find any explanation that can account for the disappearance of this line. Therefore, we identify it as the large line seen in the spectrum at 238.48 Å (line 8*), which also corresponds to an O IV line at 238.57 Å. Our CR model identifies as the most important transitions, the $2s^2 2p^4 \rightarrow 2s 2p^5$, with wavelengths in the range 300-310 Å. The convolution of the many lines appearing at this region results in five peaks, and the agreement with the experimental values is very good, better than 0.3 %. However, this preliminary model does not account very well for the relative intensities of the peaks. The strongest theoretical (HULLAC line results in 306.4 Å (line 10), which is not the higher peak of this group. Our calculations find the line 9* ($2p \rightarrow 2s$ transition) at 304.2 Å, the same position as a $2s 2p^5 \rightarrow 2s^2 2p^4$ transition of Al^{6+} (line 14* of Table 4). As displayed with a fine gray line, they overlap with a line of HeII (at 303.78 Å), which can explain the high-intensity peak in the experimental spectra.

The AS results for the spectrum at this region have been obtained in a separate calculation without mixing with higher- n configurations. The agreement with HULLAC results is remarkable. We included in this Table the measured values of 305.05 Å and 309.09 Å observed in TJ-II stellarator plasma experiments of McCarthy *et al.* [27]. However, they assigned these lines to the Al^{8+} and Al^{6+} ions, respectively. The other

experimental value marked in red is the 239.030 Å line obtained in a laser-produced plasma experiment by Valero and Goorvitch [20], assigned by these authors to Al⁶⁺.

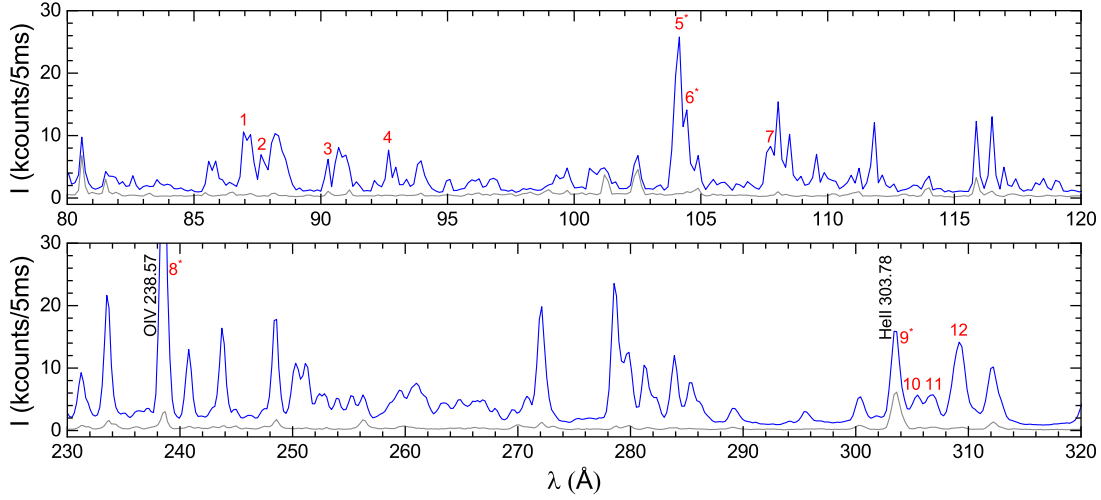


Figure 8. EAST spectrum and the lines identified as belonging to Al⁵⁺. The numbers indicate the lines (Key) described in Table 3.

Table 3. EAST experimental and theoretical lines for Al⁵⁺. The column ‘Key’ indicates the transitions labeled in Fig. 8. The reference values in red are lines assigned by the authors to other Al ions. We use the usual relativistic nomenclature $j_{\pm} \equiv l \pm \frac{1}{2}$.

Key	Exp.	FAC	HULLAC	AS	Previous Exp.	NIST	Lower	Upper
1	86.95	87.67	87.07	84.60		87.331	$(2p_{-}2p_{+}^3)_2$	$(2p_{+}^33d_{-})_3$
2	87.64	87.88	87.71	85.31	87.760 ^a	87.651	$(2p^2_{-}2p^2_{+})_2$	$(2p_{-}2p^2_{+}3d_{-})_2$
3	90.29	90.54	89.73	86.82	90.310 ^a 90.200 ^b	90.856	$(2p_{-}2p^3_{+})_2$	$(2p^2_{-}2p_{+}3d_{-})_3$
4	92.68	92.88	92.27	89.00	92.833 ^a	92.626	$(2p^2_{-}2p^2_{+})_2$	$(2p_{-}2p^2_{+}3d_{+})_2$
5*	104.15	104.55	103.58	100.71	104.196 ^a	104.046	$(2p^2_{-}2p^2_{+})_2$	$(2p_{-}2p^2_{+}3s)_3$
6*	104.45	104.84	103.86	101.04		104.464	$(2p_{-}2p^3_{+})_1$	$(2p^2_{-}2p_{+}3s)_2$
7	107.74	108.27	107.29	104.08		107.622	$(2p_{-}2p^3_{+})_2$	$(2p_{-}2p^2_{+}3s)_2$
8*	238.48	235.83	236.07	237.09	239.030 ^b		$(2s^22p_{-}2p^3_{+})_2$	$(2s2p^2_{-}2p^3_{+})_1$
9*	303.55	303.34	304.20	303.60			$(2s^22p^2_{-}2p^2_{+})_2$	$(2s2p_{-}2p^4_{+})_1$
10	305.49	304.56	306.40	306.29	305.05 ^c		$(2s^22p^2_{-}2p^2_{+})_2$	$(2s2p^2_{-}2p^3_{+})_2$
11	306.64	305.59	307.63	307.63	307.248 ^b	307.249	$(2s^22p^4_{+})_0$	$(2s2p_{-}2p^4_{+})_1$
12	309.19	306.85	308.74	309.16	309.09 ^c	309.597	$(2s^22p_{-}2p^3_{+})_1$	$(2s2p^2_{-}2p^3_{+})_2$

^a Livermore EBIT experimental results [26].

^b Laser-produced plasma experimental results [20].

^c TJ-II stellarator plasma experimental results [27].

4.4. Al^{6+}

This ion, isoelectronic to the N, has five levels in the ground configuration $1s^2 2s^2 2p^3$, separated by 14 eV. The ionization energy is 241.8 eV, and the maximum abundance is around 45 eV. For the calculation, we employ a model with 982 levels, belonging to the $2s^2 2p^2 nl$ ($n = 3, 4, 5$), $2s^2 2p 3s^2, 2s^2 2p 3p^2, 2s^2 2p 3s 3p, 2s 2p^4$ and the $2s 2p^4 nl$ ($n = 3, 4, 5$) configurations, taking into account all the mixing between these configurations. We calculated more than 48000 radiative rates and included for the collisional-radiative equations all the 982 levels. More than 500 transitions have radiative transition rates higher than 10^{11} s^{-1} in the range of wavelengths observed at EAST. The higher of them are $2s^2 2p^2 3d \rightarrow 2s^2 2p^3$, with wavelengths close to $74 \text{ \AA} - 76 \text{ \AA}$, and Einstein coefficient values of about $5 \times 10^{11} \text{ s}^{-1}$. The Al^{6+} spectrum, shown in Fig. 9, consists of a broad region between 60 \AA and 90 \AA , with many lines corresponding to transitions from $2p^2 3s$, $2p^2 3d$, $2p^2 4s$, and $2p^2 4d$ to the ground $2p^3$ levels. There is another broad region, between 230 \AA and 305 \AA , in which we can identify strong lines belonging to the $2s 2p^4 \rightarrow 2s^2 2p^3$ transitions. The most prominent line arising in the theoretical model is the line labeled in Table 4 as line 14*, whose calculated wavelength is 303.5 \AA (HULLAC). As commented above, the 303.78 \AA line identified as belonging to the HeII ion also appears at this wavelength. The other blended lines are the 2* at 63.27 \AA , which overlaps with the 3* line of Al^{8+} (Table 6), and the 6* at 80.04 \AA , which overlaps with the 4* line of Al^{7+} (Table 5). The line at 282.634 \AA observed in laser-produced plasma experiments by Valero and Goorvitch [20] is reported as belonging to the Al^{8+} , as well as the line at 284.04 \AA observed by Mc Carthy *et al.* in a stellarator plasma [27].

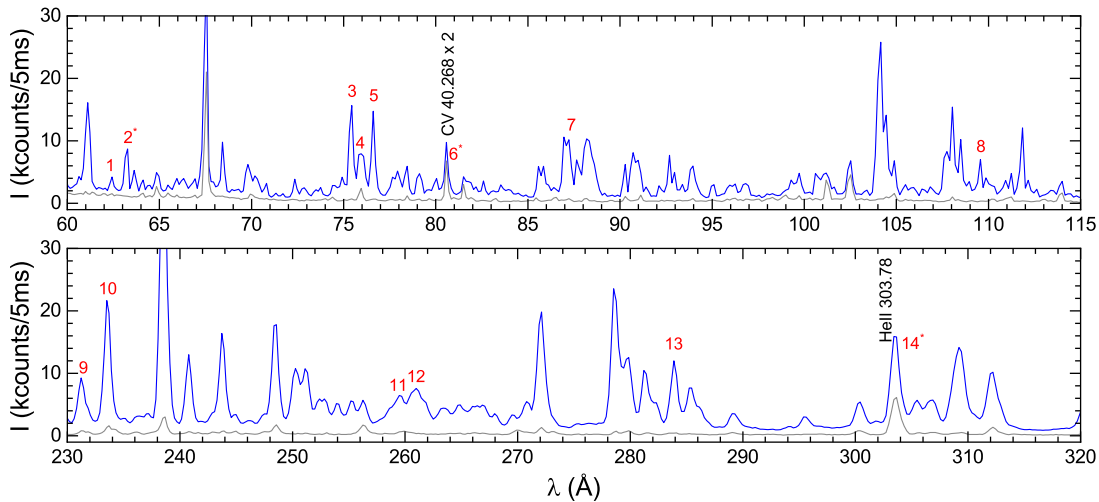


Figure 9. EAST spectrum and the lines identified as belonging to Al^{6+} . The numbers indicate the lines (Key) described in Table 4.

Table 4. EAST experimental and theoretical lines for Al⁶⁺. The column ‘Key’ indicates the transitions labeled in Fig. 9. We use the usual relativistic nomenclature $j_{\pm} \equiv l \pm \frac{1}{2}$.

Key	Exp.	FAC	HULLAC	AS	Previous Exp.	NIST	Lower	Upper
1	62.42	62.03	61.82	60.25	62.380 ^a	62.292	$(2p-2p_{+}^2)_{3/2}$	$(2p^2-4d_{+})_{5/2}$
2*	63.27	64.52	62.69	61.16	63.161 ^a	63.056	$(2p-2p_{+}^2)_{5/2}$	$(2p-2p_{+}4d_{+})_{7/2}$
3	75.43	74.89	74.55	72.39	75.434 ^a	75.367	$(2p-2p_{+}^2)_{3/2}$	$(2p^2-3d_{+})_{5/2}$
4	75.95	75.13	75.16	72.71		75.903	$(2p-2p_{+}^2)_{1/2}$	$(2p-2p_{+}3d_{+})_{3/2}$
5	76.61	76.18	75.80	73.51	76.644 ^a	76.582	$(2p-2p_{+}^2)_{5/2}$	$(2p-2p_{+}3d_{+})_{7/2}$
6*	80.04	80.35	80.03	77.17	80.043 ^a	79.928	$(2p_{+}^3)_{3/2}$	$(2p-2p_{+}3d_{+})_{5/2}$
7	87.23	87.07	87.25	86.64	87.092 ^a	87.165	$(2p-2p_{+}^2)_{3/2}$	$(2p-2p_{+}3s)_{3/2}$
8	109.56	110.29	109.73	107.60			$(2s^22p-2p_{+}3p_{+})_{5/2}$	$(2s2p-2p_{+}^3)_{5/2}$
9	231.23	229.84	230.73	231.06			$(2s^22p^2-2p_{+})_{3/2}$	$(2s2p-2p_{+}^3)_{1/2}$
10	233.50	231.37	232.27	232.95			$(2s^22p-2p_{+}^2)_{5/2}$	$(2s2p^2-2p_{+}^2)_{3/2}$
11	259.48	257.16	258.81	258.58	259.035 ^b	259.207	$(2s^22p_{+}^3)_{3/2}$	$(2s2p-2p_{+}^3)_{1/2}$
12	260.99	259.24	260.66	260.77		261.044	$(2s^22p_{+}^3)_{3/2}$	$(2s2p^2-2p_{+}^2)_{3/2}$
13	283.88	284.09	286.86	284.24	282.634 ^b 284.04 ^c	282.66	$(2s^22p_{+}^3)_{3/2}$	$(2s2p^2-2p_{+}^2)_{1/2}$
14*	303.55	303.52	303.48	300.27			$(2s^22p-2p_{+}^2)_{5/2}$	$(2s2p-2p_{+}^3)_{5/2}$

^a Livermore EBIT experimental results [26].

^b Laser-produced plasma experimental results [20].

^c TJ-II stellarator plasma experimental results [27].

4.5. Al^{7+}

This ion is isoelectronic to the C, having a ground configuration $1s^22s^22p^2$. The ionization energy is 284.6 eV, and the maximum fractional abundance is about 60 eV. Identifying the Al^{7+} spectrum is complicated due to the large number of transitions (more than 180) with values above $10^{12} s^{-1}$. However, as is shown in Fig. 10, only a few strong lines can be assigned to this ion. The atomic structure included in the model consists of the $2s^22pnl$ ($n = 3, 4, 5$), $2s2p3n^2$ ($n = 3, 4$), $2s2p^3$ and the $2s2p^2nl$ ($n = 3, 4, 5$) configurations, taking into account all the mixing between these configurations, totalizing 833 levels and about 40000 transitions. The CR model allows us to identify the dominant lines listed in the Table 5. Most of the strong transitions are in the range 50 Å to 75 Å, mainly corresponding to the $2s2p3d^2 \rightarrow 2s2p^23d$ and $2p3d \rightarrow 2p^2$ transitions. There are also prominent lines corresponding to the $2s2p^3 \rightarrow 2s^22p^2$, with wavelengths in the range 235-330 Å, particularly lines 8 and 10. We have added $n = 6$ and $n = 7$ to investigate the effect of mixing configurations in improving the theoretical model, but this has not produced significant changes in the results. For example, the theoretical value obtained for the strong line 10 by a HULLAC calculation including only $n = 3, 4, 5$ is 335.8 Å, while the improvement obtained by adding $n = 6, 7$ (335.5 Å) is still insufficient to bring the value closer to the experimental result of 332.51 Å. It is noticeable that this line has also been identified in a stellarator plasma by McCarthy *et al.* [27], but as belonging to the Al^{9+} ion. We included in the Table other lines observed in laser-produced plasma experiments by Valero and Goorvitch [20], although most of them are labeled in red since the authors assign these lines to other ions. According to them, line 240.770 Å corresponds to Al^{6+} , line 243.760 Å corresponds to Al^{5+} , and line 278.699 Å corresponds to the Al^{4+} ion. We have marked with an asterisk, in addition to line 4*, lines 1* and 7* because in the first case, the peak overlaps with a high-intensity second-order C VI line (2×33.73 Å), and in the second, the 7* line overlaps with an O III line at 248.32 Å.

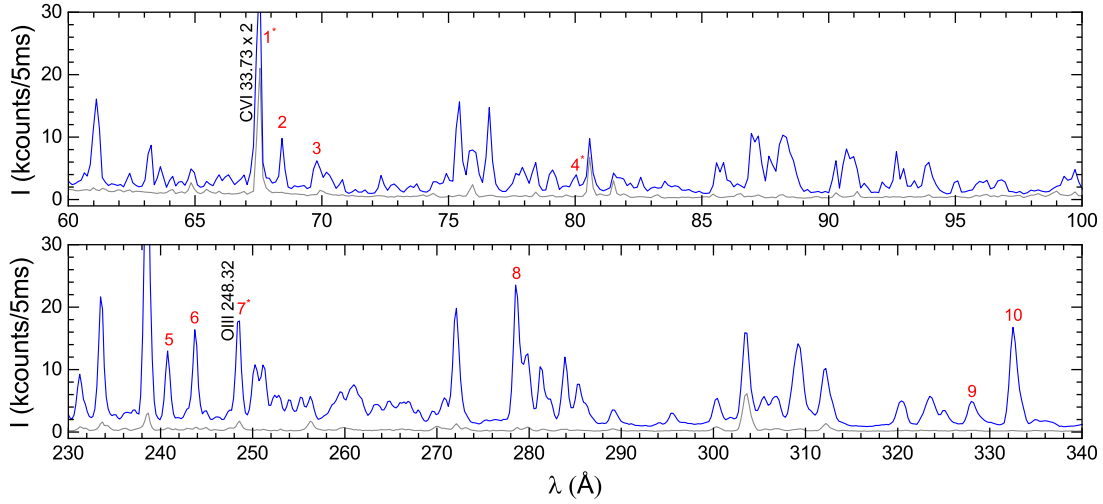


Figure 10. EAST spectrum and the lines identified as belonging to Al^{7+} . The numbers indicate the lines (Key) described in Table 5.

Table 5. EAST experimental and theoretical lines for Al^{7+} . The column ‘Key’ indicates the transitions labeled in Fig. 10. We use the usual relativistic nomenclature $j_{\pm} \equiv l \pm \frac{1}{2}$.

Key	Exp.	FAC	HULLAC	AS	Previous Exp.	NIST	Lower	Upper
1*	67.68	67.51	66.92	65.43	67.440 ^a	67.946	$(2p_{+}^2)_2$	$(2p_{+}3d_{+})_3$
2	68.43	68.41	67.81	66.15	68.446 ^a 68.375 ^b	68.375	$(2p_{-}2p_{+})_2$	$(2p_{+}3d_{-})_3$
3	69.81	70.39	69.75	69.45	69.726 ^a	70.161	$(2p_{-}2p_{+})_2$	$(2p_{+}3d_{-})_2$
4*	80.04	80.55	80.03	80.11	80.514 ^a	80.320	$(2s^22p_{-}2p_{+}^2)_3$	$(2s^22p_{+}^23s)_2$
5	240.78	241.49	242.75	243.63	240.770 ^b		$(2s^22p_{-}2p_{+})_1$	$(2s^22p_{-}2p_{+}^2)_1$
6	243.71	244.98	244.48	244.75	243.760 ^b		$(2s^22p_{+}^2)_2$	$(2s^22p_{-}2p_{+}^2)_1$
7*	248.45	248.99	249.16	249.66		248.456	$(2s^22p_{-}2p_{+})_2$	$(2s^22p_{+}^3)_1$
8	278.53	277.57	281.48	281.58	278.699 ^b		$(2s^22p_{-}2p_{+})_2$	$(2s^22p_{-}2p_{+}^2)_2$
9	327.98	328.64	332.26	327.98		382.200	$(2s^22p_{-}2p_{+})_1$	$(2s^22p_{+}^3)_2$
10	332.51	333.52	335.51	331.50	332.79 ^c		$(2s^22p_{+}^2)_2$	$(2s^22p_{+}^3)_2$

^a Livermore EBIT experimental results [26].

^b Laser-produced plasma experimental results [20].

^c TJ-II stellarator plasma experimental results [27].

4.6. Al^{8+}

The ground configuration of the B-like Al^{8+} ion is $1s^2 2s^2 2p$. Its ionization energy is 330.2 eV, and the maximum abundance is around 75 eV. The higher transition probabilities are from radiative processes of the type $3d \rightarrow 2p$, in particular, the $2s3d^2 \rightarrow 2s2p3d$ around the 57 Å, and the $2s2p3d \rightarrow 2s2p^2$ in the 60-64 Å range, with radiative rate coefficients higher than 10^{12} s^{-1} . The atomic structure considered in our theoretical model consists of the $2s^2 nl$ ($n = 3, 4, 5$), $2s2p^2$, $2s nl^2$ ($n = 3, 4$), and the $2s2pnl$ ($n = 3, 4, 5$) configurations, including all the mixing between these configurations. The resultant structure has 281 levels and more than 6000 radiative transitions, and the spectra lines identified for this ion are shown in Fig. 11. With our preliminary CR model, we were able to determine that in the spectrum of this ion, line 2 in Table 6 ($3d \rightarrow 2p$) stands out for its intensity. In the 280-290 Å range, a group of high-intensity peaks is recognized both in the experimental and theoretical spectra (as $2p \rightarrow 2s$), labeled in the Table as 5 to 8, and the same transitions provide the high-intensity peaks 9 and 10. As mentioned before, line 3* overlaps with line 2* of Al^{6+} . Line 1* stands in the same wavelength as line 4* (Table 7) of Al^{9+} . Two experimental results from laser-produced plasmas [20] agree very well with our values (lines 6 and 9), but Valero and Goorvitch identified the lines as belonging to Al^{4+} and Al^{4+} , respectively. The theoretical results given by the three codes show similar patterns. However, using a complete CR model, an exhaustive analysis is required to elucidate the spectra in this region accurately.

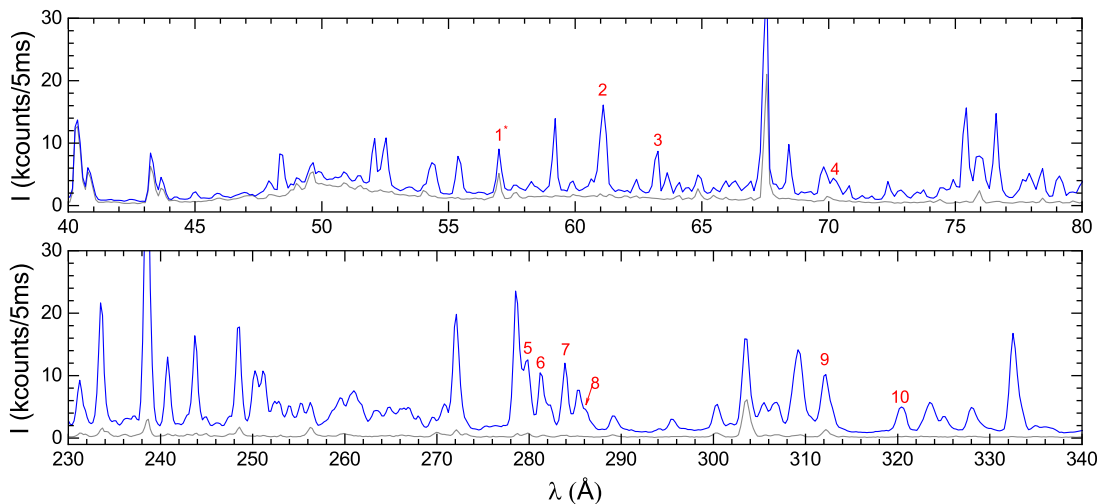


Figure 11. EAST spectrum and the lines identified as belonging to Al^{8+} . The numbers indicate the lines (Key) described in Table 6.

Table 6. EAST experimental and theoretical lines for Al⁸⁺. The column ‘Key’ indicates the transitions labeled in Fig. 11. We use the usual relativistic nomenclature $j_{\pm} \equiv l \pm \frac{1}{2}$.

Key	Exp.	FAC	HULLAC	AS	Previous Exp.	NIST	Lower	Upper
1*	56.99	57.53	57.29	57.01	56.957 ^a	56.945	(2s ² 2p ₊) _{3/2}	(2s2p ₊ 3p ₋) _{5/2}
2	61.10	61.20	60.63	60.07	61.014 ^a	61.078	(2s ² 2p ₊) _{3/2}	(2s ² 3d ₊) _{5/2}
3*	63.27	63.69	63.56	62.78	63.627 ^a 63.509 ^b	63.025	(2s2p ₋ 2p ₊) _{5/2}	(2s2p ₊ 3d ₋) _{7/2}
4	70.18	69.78	69.54	68.61	69.818 ^a	69.716	(2s2p ₋ 2p ₊) _{5/2}	(2s2p ₊ 3s) _{3/2}
5	279.86	283.22	281.55	283.89		280.114	(2s ² 2p ₋) _{1/2}	(2s2p ₊ ²) _{3/2}
6	281.42	285.62	283.99	286.70	281.433 ^b	282.407	(2s ² 2p ₋) _{1/2}	(2s2p ₋ 2p ₊) _{1/2}
7	283.88	287.28	285.53	288.45	284.04 ^c	284.015	(2s ² 2p ₊) _{3/2}	(2s2p ₊ ²) _{3/2}
8	286.13	289.76	288.03	291.35	286.364 ^c	286.364	(2s ² 2p ₊) _{3/2}	(2s2p ₋ 2p ₊) _{1/2}
9	312.21	313.48	313.46	312.11	312.241 ^b		(2s ² 2p ₋) _{1/2}	(2s2p ₊ ²) _{1/2}
10	320.41	318.47	318.39	317.63		321.027	(2s ² 2p ₊) _{3/2}	(2s2p ₊ ²) _{1/2}

^a Livermore EBIT experimental results [26].

^b Laser-produced plasma experimental results [20].

^c TJ-II stellarator plasma experimental results [27].

4.7. Al^{9+}

The Be-like ion Al^{9+} has a simple atomic structure in which the $1s^2 2s^2$ is the ground level. The ionization energy is 398.7 eV, and the temperature of maximum abundance is around 90 eV. There are fewer than 30 transitions with radiative rate coefficients greater than 10^{12} s^{-1} , and they are mainly $2snl \rightarrow 2s2p$ (between 38 Å to 45 Å) and $2pnl \rightarrow 2p^2$ (between 56 Å to 60 Å). Only two transitions to the ground level have high Einstein coefficients, these are the lines labeled 2 and 6 in Table 7, $3p \rightarrow 2s$ and $2p \rightarrow 2s$, respectively. The spectral lines corresponding to this ion are marked in Fig. 12. To identify the lines, we performed a simple CR model calculation, in which we included the $2snl$ ($n = 3, 4, 5$), $2p^2$, $3s^2$, $4p^2$, $4d^2$, $5s^2$, $2s2p$ and the $2p3l$ ($l = 0, 1, 2$) configurations, taking into account all the mixing between these configurations. The resultant system has 94 levels and more than 800 transitions. Our calculations show that only the six lines listed in the Table are produced by radiative emission of the Al^{9+} ion. The first line listed (1* at 43.24 Å) overlaps with the second-order OVII line (2×21.6 Å), and line 4* overlaps with line 1* of Table 6 corresponding to Al^{8+} . The theoretical intensity of line 6 ($2s2p \rightarrow 2s^2$, with wavelengths close to 324 Å) is enormous in both HULLAC and AS calculations. The EAST experimental spectra only show a small intensity and broad peak, very different than those predicted by our calculations. No other experimental works reported a striking line in this region. We do not have any explanation for a possible quenching of this line. Perhaps, a more elaborated CR model can help to understand the physical mechanisms ruled in this spectral region.

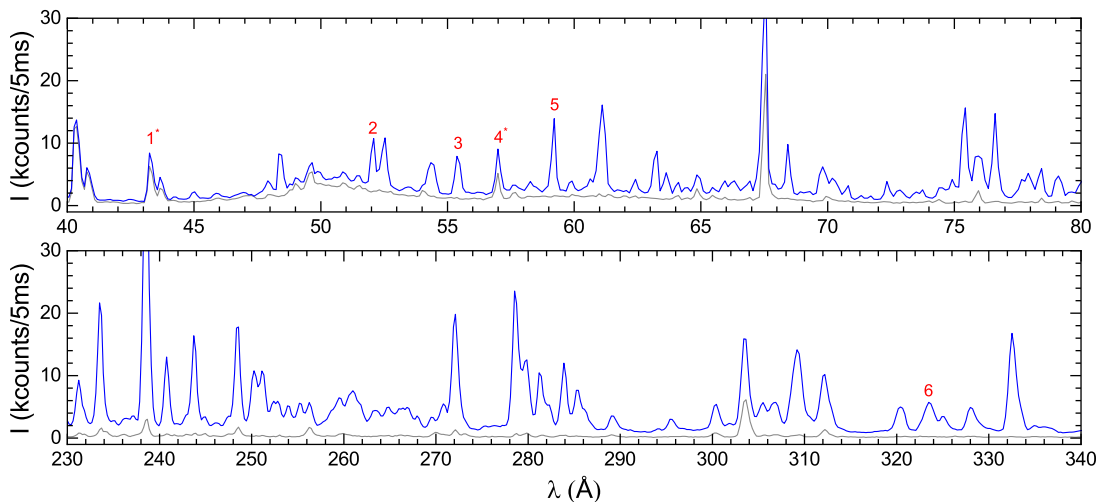


Figure 12. EAST spectrum and the lines identified as belonging to Al^{9+} . The numbers indicate the lines (Key) described in Table 7.

Table 7. EAST experimental and theoretical lines for Al⁹⁺. The column ‘Key’ indicates the transitions labeled in Fig. 12.

Key	Exp.	FAC	HULLAC	AS	Previous Exp.	NIST	Lower	Upper
1*	43.24	42.43	42.38	42.28			(2s2p ₊) ₂	(2s4d ₊) ₃
2	52.09	52.89	51.93	51.80	51.975 ^a	51.979	2s ²	(2s3p ₋) ₁
3	55.38	55.37	55.33	55.18	55.318 ^a	55.376	(2s2p ₊) ₂	(2s3d ₊) ₃
4*	56.99	56.96	57.13	56.82	56.957 ^a	56.945	(2p ₊ ²) ₂	(2p ₊ 3d ₊) ₃
5	59.21	59.35	59.19	59.02	59.094 ^a 59.107 ^b	59.298	(2s2p ₊) ₁	(2s3d ₊) ₂
6	323.47	322.94	323.78	323.51			2s ²	(2s2p ₊) ₁

^a Livermore EBIT experimental results [26].

^b Laser-produced plasma experimental results [20].

4.8. Al^{10+}

This ion, isoelectronic to the Li (ground $1s^2 2s$), has a straightforward atomic structure and a few radiative lines, as is shown in Fig. 13. The ionization energy is 442 eV, and the maximum abundance is about 116 eV. We implemented a simple CR model, with only 24 levels belonging to the $1s^2 nl$ ($n = 2, 3, 4, 5$) configurations, including all the mixing between them, resulting in 78 dipole-allowed radiative transitions. Table 8 resumes the three dominant lines that appear highly in the spectra. The agreement between the three different calculations and the experimental results is excellent. In particular, HULLAC results are closer than 0.2% from the measured values.

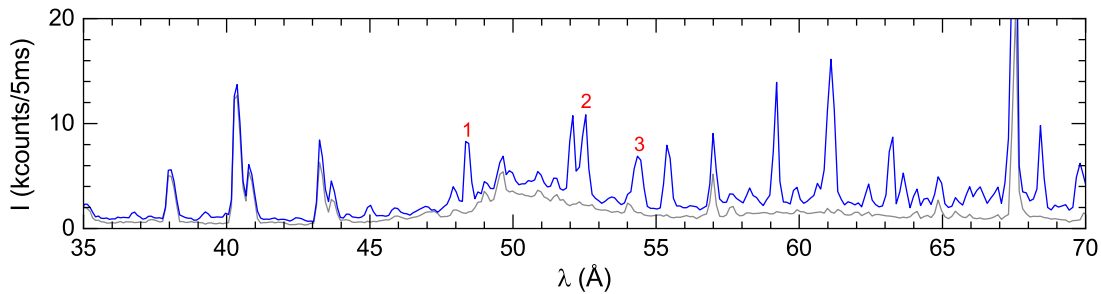


Figure 13. EAST spectrum and the lines identified as belonging to Al^{10+} . The numbers indicate the lines (Key) described in Table 3.

Table 8. EAST experimental and theoretical lines for Al^{10+} . The column ‘Key’ indicates the transitions labeled in Fig. 13.

Key	Exp.	FAC	HULLAC	AS	Previous Exp.	NIST	Lower	Upper
1	48.34	48.29	48.35	48.27	48.330 ^a	48.297	2s	3p ₋
2	52.54	52.44	52.49	52.45	52.438 ^a	52.446	2p ₊	3d ₊
3	54.35	54.41	54.43	54.41	54.219 ^a	54.388	2p ₊	3s

^a Livermore EBIT experimental results [26].

4.9. Al^{11+} and Al^{12+}

The Al^{11+} ion is isoelectronic to He (ground configuration $1s^2$). Therefore, it has relatively considerable ionization energy (2086 eV) and is the dominant ion along a broad range of temperatures, roughly 70 to 1000 eV. In the EAST experiment, only the $K\alpha$ lines have been detected at the low edge of the wavelengths that our instruments can measure. The $1s3p \rightarrow 1s^2$ and $1s4p \rightarrow 1s^2$ lines should appear at 6.6 Å and 6.3 Å, but these can not be distinguished from the background. For calculating the atomic structure, we included mixing between the $1snl$ ($n = 2, 3, 4, 5$) configurations, obtaining very accurate results, as shown in Table 9.

Concerning the H-like ion Al^{12+} , only the $K\alpha_1$ and $K\alpha_2$ lines are visible in the EAST spectra, but these are not fully resolved in our measurements, so they appear as a unique peak at 7.18 Å. For the theoretical model, we included the nl ($n = 2, 3, 4, 5$) configurations, allowing us to accurately calculate the wavelengths. The lines indicated in the Table, have also been observed in laser-produced plasma experiments [23, 24, 21, 22, 25], in excellent agreement with our values.

Table 9. EAST experimental and theoretical lines for Al^{11+} and Al^{12+} .

Ion	Exp.	FAC	HULLAC	AS	Previous Exp.	NIST	Lower	Upper
Al^{12+}		7.171	7.171	7.169	7.1703 ^a 7.17 ^{b,c}	7.171	1s	2p ₊
	7.18	7.176	7.176	7.174	7.1759 ^a	7.177	1s	2p ₋
Al^{11+}		7.759	7.754	7.769	7.75 ^d	7.758	1s ²	(1s2p ₊) ₁
	7.80	7.812	7.809	7.820	7.80 ^d 7.81 ^e	7.807	1s ²	(1s2p ₋) ₁

^a Laser produced plasma experimental results [23].

^b Laser produced plasma experimental results [24].

^c Laser produced plasma experimental results [25].

^d Laser produced plasma experimental results [21].

^e Laser produced plasma experimental results [22].

5. Summary

Extreme ultraviolet (EUV) spectra emitted from aluminum ions in the 5–340 Å wavelength range were observed in Experimental Advanced Superconducting Tokamak (EAST) discharges. We use three different atomic computational codes, FAC, HULLAC, and AUTOSTRUCTURE, to identify the lines observed in our measurements. The identification could be made by using a preliminary version of a model collisional-radiative code that will be presented in a forthcoming work in its final form. It will include other processes besides the collisional excitations, deexcitations, and radiative transitions between the levels of each ion. Overall, we found that the three codes can reproduce the experimental wavelengths with very good accuracy. Especially if consider that the calculations have been made without any additional adjustments since our objective has been to evaluate the capabilities of these codes. The performance of the HULLAC code is particularly remarkable, which in many cases reproduces the experimental values with errors less than 0.3%.

6. Acknowledgments

This work was supported by the National MCF Energy R & D Program (Nos. 2022YFE03180400, 2019YFE030403, 2018YFE0311100), National Natural Science Foundation of China (Grant Nos. 12322512, 11905146, 11975273) and Chinese Academy of Sciences President’s International Fellowship Initiative (PIFI) (No. 2020VMA0001). DM acknowledges partial support from CONICET by Project No. PIP11220200102421CO, and the ANPCyT by Project No. PICT- 2020-SERIE A-01931 in Argentina, and the Alliance of International Science Organizations (ANSO) Visiting Fellowship (ANSO-VF-2021-03), in China.

7. References

- [1] R. A. Langley, J. Bohdansky, W. Eckstein, P. Mioduszewski, J. Roth, E. Taglauer, E. Thomas, H. Verbeek, and K. Wilson, “Data compendium for plasma-surface interactions,” *Nuclear Fusion*, vol. 24, no. S1, p. 001, 1984.
- [2] W. Eckstein, J. Bohdansky, and J. Roth, “Physical sputtering,” *Nuclear Fusion*, vol. 1, p. 51, 1991.
- [3] X. Zhao, B. Xiao, A. J. Fletcher, K. M. Thomas, D. Bradshaw, and M. J. Rosseinsky, “Hysteretic adsorption and desorption of hydrogen by nanoporous metal-organic frameworks,” *Science*, vol. 306, no. 5698, pp. 1012–1015, 2004.
- [4] S. Wu and EAST team, “An overview of the EAST project,” *Fusion Engineering and Design*, vol. 82, no. 5-14, pp. 463–471, 2007.
- [5] B. Wan, Y. Liang, X. Gong, J. Li, N. Xiang, G. Xu, Y. Sun, L. Wang, J. Qian, and H. Liu, “Overview of EAST experiments on the development of high-performance steady-state scenario,” *Nuclear Fusion*, vol. 57, no. 10, p. 102019, 2017.
- [6] B. Wan, Y. Liang, X. Gong, N. Xiang, G. Xu, Y. Sun, L. Wang, J. Qian, H. Liu, and L. Zeng, “Recent advances in EAST physics experiments in support of steady-state operation for ITER and CFETR,” *Nuclear Fusion*, vol. 59, no. 11, p. 112003, 2019.

- [7] B. Wan, X. Gong, Y. Liang, N. Xiang, G. S. Xu, Y. Sun, L. Wang, J. Qian, H. Liu, and B. Zhang, “Advances in the long-pulse steady-state high beta H-mode scenario with active controls of divertor heat and particle fluxes in EAST,” *Nuclear Fusion*, vol. 62, no. 4, p. 042010, 2022.
- [8] Y. Song, X. Peng, H. Xie, X. Liu, L. Bao, Z. Zhou, L. Cao, T. Xu, X. Ji, and Y. Peng, “Plasma facing components of EAST,” *Fusion Engineering and Design*, vol. 85, no. 10-12, pp. 2323–2327, 2010.
- [9] C. Liu, L. Zhang, L. Cao, L. Li, L. Han, Z. Wang, H. Xu, Y. Liu, L. Liu, D. Yao, *et al.*, “Current status and upgrade activities on the guard limiter of 4.6 GHz lower hybrid antennas for EAST Tokamak,” *Fusion Engineering and Design*, vol. 125, pp. 93–97, 2017.
- [10] L. Zhang, L. Cao, D. Yao, L. Han, Z. Wang, L. Li, Y. Liu, and C. Liu, “A tungsten guard limiter for EAST 4.6 GHz lower hybrid waveguide antennas,” *Fusion Engineering and Design*, vol. 136, pp. 447–453, 2018.
- [11] C. Hu, W. Zhang, Y. Xu, S. Liu, and L. Yu, “Analysis of shine-through of EAST neutral beam,” *High Power Laser and Particle Beams*, vol. 27, no. 12, p. 126001, 2015.
- [12] N. Yan, V. Naulin, G. Xu, J. J. Rasmussen, H. Wang, S. Liu, L. Wang, Y. Liang, A. H. Nielsen, and J. Madsen, “Langmuir-magnetic probe measurements of elms and dithering cycles in the east tokamak,” *Plasma physics and controlled fusion*, vol. 56, no. 9, p. 095023, 2014.
- [13] L. Meng, J. Xu, J. Liu, L. Cao, P. Wang, A. Li, L. Yu, G. Xu, and L. Wang, “Development of Langmuir probe array for the new lower tungsten divertor in EAST,” *Fusion Engineering and Design*, vol. 175, p. 113011, 2022.
- [14] H. Lan, T. Shi, N. Yan, X. Li, S. Li, R. Chen, M. Duan, G. Hu, L. Liu, and W. Zhang, “A new electromagnetic probe array diagnostic for analyzing electrostatic and magnetic fluctuations in EAST plasmas,” *Plasma Science and Technology*, vol. 25, no. 7, p. 075105, 2023.
- [15] L. Li, L. Zhang, Z. Xu, S. Morita, Y. Cheng, F. Zhang, W. Zhang, Y. Duan, Q. Zang, S. Wang, S. Dai, G. Zuo, Z. Sun, L. Wang, X. Ding, J. Qian, H. Liu, and L. Hu, “Line identification of extreme ultraviolet (EUV) spectra from low-Z impurity ions in EAST Tokamak plasmas,” *Plasma Science and Technology*, vol. 23, no. 7, p. 075102, 2021.
- [16] L. Zhang, S. Morita, Z. Wua, Z. Xu, X. Yang, Y. Cheng, Q. Zang, H. Liu, Y. Liu, H. Zhang, T. Ohishi, Y. Chen, L. Xu, C. Wu, Y. Duan, W. Gao, J. Huang, X. Gong, and L. Hu, “A space-resolved extreme ultraviolet spectrometer for radial profile measurement of tungsten ions in the Experimental Advanced Superconducting Tokamak,” *Nuclear Instruments & Methods in Physics Research*, vol. 916, no. FEB.1, pp. 169–178, 2019.
- [17] W. Zhang, L. Zhang, Y. Cheng, S. Morita, Z. Wang, A. Hu, F. Zhang, Y. Duan, T. Zhou, S. Wang, and H. Liu, “Line identification of extreme ultraviolet (EUV) spectra from iron, copper and molybdenum ions in EAST Tokamak,” *Physica Scripta*, vol. 97, no. 4, p. 045604 (25pp), 2022.
- [18] L. Zhang, S. Morita, Z. Xu, Z. Wu, P. Zhang, C. Wu, W. Gao, T. Ohishi, M. Goto, and J. Shen, “A fast-time-response extreme ultraviolet spectrometer for measurement of impurity line emissions in the Experimental Advanced Superconducting Tokamak,” *Review of Scientific Instruments*, vol. 86, no. 12, p. 123509, 2015.
- [19] Z. Xu, L. Zhang, Y. Cheng, S. Morita, L. Li, W. Zhang, F. Zhang, Z. Zhao, T. Zhou, Z. Wu, X. Lin, X. Gao, X. Ding, Y. Yang, and H. Liu, “An extreme ultraviolet spectrometer working at 10–130 Å for tungsten spectra observation with high spectral resolution and fast-time response in Experimental Advanced Superconducting Tokamak,” *Nuclear Instruments and Methods in Physics Research, A*, vol. 1010, p. 165545, 2021.
- [20] F. P. Valero and D. Goorvitch, “The spectra of highly ionized Aluminum,” *The Astrophysical Journal*, vol. 178, pp. 271–276, 1972.
- [21] V. Boiko, A. Y. Chugunov, T. Ivanova, A. Y. Faenov, I. Holin, S. Pikuz, A. Urnov, L. Vainshtein, and U. Safronova, “He-like ion resonance-line satellites radiated from Be-like ions,” *Monthly Notices of the Royal Astronomical Society*, vol. 185, no. 2, pp. 305–324, 1978.
- [22] V. Shlyaptsev, G. Avaria, M. Grisham, J. Li, F. Tomasel, M. Busquet, and J. Rocca, “Capillary discharge X-ray lasers: The quest for sub-10 nm lasers,” in *X-Ray Lasers 2014: Proceedings of*

- the 14th International Conference on X-Ray Lasers*, pp. 103–112, Springer, 2016.
- [23] V. A. Boiko, F. A. Ya., S. A. Pikuz, and U. I. Safranova, “The analysis of satellites to the H-like ion resonance lines observed in the X-ray region,” *Monthly Notices of the Royal Astronomical Society*, no. 2, pp. 107–120, 1977.
- [24] J. Couturaud, “Spectroscopic study of laser created aluminum plasma,” *Optics Communications*, vol. 22, no. 1, pp. 71–74, 1977.
- [25] C. Kaur, S. Chaurasia, A. K. Poswal, D. S. Munda, A. K. Rossall, M. N. Deo, and S. M. Sharma, “K-shell X-ray spectroscopy of laser produced aluminum plasma,” *Journal of Quantitative Spectroscopy and Radiative Transfer*, vol. 187, pp. 20–29, 2017.
- [26] M. Gu, P. Beiersdorfer, and J. Lepson, “Emission line spectra of Al IV–Al XI in the extreme ultraviolet region 40–170 Å,” *The Astrophysical Journal*, vol. 732, no. 2, p. 91, 2011.
- [27] K. McCarthy, B. Zurro, E. Hollmann, J. H. Sanchez, *et al.*, “A spectral line survey from 17.5–250 nm of plasmas created in a magnetic confinement device,” *Physica Scripta*, vol. 91, no. 11, p. 115601, 2016.
- [28] Y. Song, B. Wan, X. Gong, J. Li, X. Wu, F. Liu, J. Chen, J. Hu, G. Xu, and K. Lu, “Recent EAST Experimental Results and Systems Upgrade in Support of Long-Pulse Steady-State Plasma Operation,” *IEEE Transactions on Plasma Science*, vol. 50, no. 11, pp. 4330–4334, 2022.
- [29] X. Han, A. Hu, D. Li, S. Xiao, B. Tian, Q. Zang, J. Zhao, C. Hsieh, X. Gong, L. Hu, *et al.*, “Multiple laser system for high-resolution Thomson scattering diagnostics on the EAST Tokamak,” *IEEE Transactions on Plasma Science*, vol. 46, no. 2, pp. 406–409, 2018.
- [30] Y. Wang, T. Zhang, X. Liu, C. Zhao, H. Qu, G. Li, M. Wu, K. Ye, F. Wen, H. Xiang, *et al.*, “Development of the quasi-optical combiner systems for density profile reflectometers on the EAST Tokamak,” *Fusion Engineering and Design*, vol. 148, p. 111286, 2019.
- [31] M. Klapisch, J. L. Schwob, B. S. Fraenkel, and J. Oreg, “The 1s-3p $K\beta$ -like X-ray spectrum of highly ionized iron,” *J. Opt. Soc. Am.*, vol. 67, no. 2, pp. 148–155, 1977.
- [32] A. Bar-Shalom, M. Klapisch, and J. Oreg, “HULLAC, an integrated computer package for atomic processes in plasmas,” *Journal of Quantitative Spectroscopy and Radiative Transfer*, vol. 71, no. 2-6, pp. 169–188, 2001.
- [33] N. R. Badnell, “Dielectronic recombination of Fe^{22+} and Fe^{21+} ,” *Journal of Physics B: Atomic and Molecular Physics*, vol. 19, no. 22, p. 3827, 1986.
- [34] N. R. Badnell, “On the effects of the two-body non-fine-structure operators of the Breit-Pauli Hamiltonian,” *Journal of Physics B: Atomic, Molecular and Optical Physics*, vol. 30, no. 1, p. 1, 1997.
- [35] N. R. Badnell, “A Breit-Pauli distorted wave implementation for AUTOSTRUCTURE,” *Computer Physics Communications*, vol. 182, no. 7, pp. 1528–1535, 2011.
- [36] M. F. Gu, “The Flexible Atomic Code,” *Can. J. Phys.*, vol. 86, no. 5, pp. 675–689, 2008.